

Hybrid - block copolymer nanocomposites. characterization of nanostructure by small-angle X-ray scattering (SAXS)*

A. Romo-Uribe

Laboratorio de Nanopolímeros y Coloides, Instituto de Ciencias Físicas, Universidad Nacional Autónoma de México, Av. Universidad s/n, Cuernavaca, Mor. 62210 MÉXICO, e-mail: ARomo-Uribe@fis.unam.mx

Recibido el 19 de abril de 2006; aceptado el 16 de abril de 2007

The nanoscopic order of a series of block copolymer-inorganic nanocomposites was characterized using small-angle X-ray scattering (SAXS). The nanostructures were obtained via a diblock copolymer directed sol-gel synthesis. The copolymer consists of blocks of poly(isoprene) -PI- and blocks of poly(ethylene oxide) -PEO. The inorganic material consists of a crosslinked sol of 3-glycidoxypropyltrimethoxysilane and aluminum-tri-sec-butoxide in a 4:1 mole ratio, to generate an aluminosilicate ceramic. The PEO block is swollen by the ceramic precursor and acts as a nanoreactor for their sol-gel synthesis. The resulting nanostructured hybrid has PI as the majority phase. Two series of nanocomposites, designated PI-b-PEO-D and PI-b-PEO-E, were studied; these correspond to 15 wt% PEO and 13 wt% PEO, respectively. The results showed that the nanoscale order characteristic of block copolymers (lamellar, spherical, and cubic) is not only achieved in these hybrid nanocomposites, but the molecular assembly offers the possibility of being utilized as a template for highly ordered inorganic nanostructures. The amount of inorganic nanofiller and the molecular weight of the blocks define the type of morphology assumed by the nanostructure.

Keywords: Nanocomposites; hybrid polymers; block copolymers; microstructure; X-ray scattering.

Se caracterizó el orden nanoscópico por medio de difracción de rayos X a bajo ángulo (SAXS) de una serie de nanocompuestos inorgánicos-copolímeros de bloque. Las nanoestructuras se obtuvieron via síntesis de sol-gel dirigida por copolímero de bloque. El copolímero está formado por bloques de poli-isopreno (PI) y bloques de poli-óxido de etileno (PEO). El material inorgánico consiste en un sol vulcanizado de 3-glycidoxypropyltrimethoxysilano y de tri-sec-butoxido de aluminio a razón molar de 4:1, para generar un cerámico de aluminosilicato. El bloque de PEO es hinchado por el precursor cerámico y actúa como nanoreactor para la síntesis sol-gel. El híbrido nanoestructurado resultante tien poli-isopreno como fase predominante. Se estudiaron dos series de nanocompuestos, designados PI-b-PEO-D y PI-b-PEO-E, los cuales contienen 15 % g/g PEO y 13 % g/g PEO, respectivamente. Los resultados muestran que el orden nanoescalar característico de copolímeros en bloque (lamelar, esférico o cúbico) también se obtiene en estos nanocompuestos híbridos, y además el ensamblaje molecular ofrece la posibilidad de ser utilizado como un templete para obtener nanoestructuras altamente ordenadas. La concentración del nanocompuesto inorgánico, así como el peso molecular de los bloques en el copolímero, definen el tipo de morfología de las nanoestructuras.

Descriptores: Nanocompuestos; polimeros híbridos; copolimeros en bloque; microestructura; difracción de rayos X.

PACS: 81.05.Lg; 83.80.Uv; 81.07.-b; 61.46.-w; 82.80.Ej

1. Introduction

Polymer nanocomposites are constructed by dispersing nanofiller material into a polymeric matrix. Different types of nanofillers are currently utilized, for instance, nanoclays, carbon nanotubes, hybrid organic-inorganic nanoparticles and polyhedral silsesquioxane (POSS). There are three common methods for producing polymer nanocomposites: melt compounding, in-situ polymerization and the solvent method [1,2].

Another approach is the use of block copolymers of high molecular weight to make the transition from the small to the large mesoscopic regime of silica-type nanostructures [3]. In other words, organic structures formed through self-assembly can be utilized as structure-directing agents. The final morphology is then determined by the cooperative organization of inorganic and organic molecular species into three-dimensionally structured arrays, a concept also discussed in the context of biomineralization [4]. This strategy has already been successfully used in the preparation of inorganic mesoporous materials [5]. These materials could also find applica-

tions in catalysis, membrane and separation technology, and molecular engineering [6,7].

Block copolymers are the basis of products such as adhesives, asphalt additives, and upholstery foams. Joining two or more chemically distinct polymer blocks, each a linear series of identical monomers that may be thermodynamically incompatible produces this class of macromolecules. Segregation of these blocks on the molecular scale (5–100 nm) can produce a variety of complex nanostructures [8].

All block copolymers belong to a broad category of condensed matter sometimes referred to as “soft materials”. These soft materials, in contrast to crystalline solids, are characterized by fluid-like disorder on the molecular scale and a high degree of order at longer length scales. Their complex structure is correlated with their properties, for instance, polyurethane foams are composed of multiblock copolymers known as thermoplastic elastomers, which combine high-temperature resilience and low-temperature flexibility. Pressure-sensitive adhesives are based on linear triblock copolymers. Moreover, the addition of block copoly-

mers to commodity plastics, such as polystyrene, can enhance toughness, or modify the surface properties for applications as diverse as colloidal stabilization, medical implantation, and microelectronic fabrication. Recent advances in synthetic chemistry enable the combination of multiple blocks in novel molecular architectures to produce structured materials endowed with tailored mechanical, optical, electrical, ionic, barrier, and other physical properties [9].

As stated above, modern synthetic techniques make the production of a wide variety of block configurations possible. In the context of the present research, a basic and limited classification of these molecular structures is illustrated in Fig. 1. The classification is based on two parameters: (1) the number of chemically distinct blocks, and (2) linear versus branched sequencing of the blocks.

The simplest and most studied architecture is the linear AB diblock, consisting of long sequences of type A monomers covalently bonded to a chain of type B monomers. ABA triblocks and (AB)_n multiblocks are formed by coupling additional A and B blocks. The use of three or more monomer types during polymer synthesis leads to the production of ABC or other multicomponent molecular architectures. Moreover, subtle variations in the molecular topology, for instance, ABC vs. ACB, or star-ABC, can lead to pronounced changes in morphology as well as material properties [9,10].

Note, however, that in most chemical synthesis reactions, normal chemical kinetics results in a distribution of molecular weights, and in block copolymers this results in compositional heterogeneity. This is normally the case for commercially relevant block copolymers [10].

The unique properties, and therefore the applications of block copolymers, rely critically on their nanoscopic self-assembly (~ 10 nm scale) in the molten and solid states. The collective self-assembly produces spatially periodic composition patterns that can exhibit considerable complexity. The

patterns are commonly referred to as microphases, mesophases or nanophases, depending on the length scale [9].

A series of hybrid block copolymer-inorganic nanostructures obtained via a sol-gel process were studied using small-angle X-ray scattering (SAXS). SAXS is a technique that has been particularly suitable for elucidating the nanomorphology adopted by the microphase separation typical of these complex materials. The results show that the different morphologies adopted by these hybrid nanofillers, say, lamellar, cylindrical hexagonal, and cubic spherical, are driven by the amount of hybrid material. The morphology of microdomains formed by pure and simple diblock copolymers with only dispersive interactions at a segregation limit is now well understood [9]. The block copolymer-inorganic nanostructures characterized here extend such studies as the morphology is expected to be rich, though in a sense more complicated than the pure copolymer system [3,11,12].

2. Experimental

2.1. Samples

A diblock polyisoprene-b-polyethylene oxide (PI-b-PEO) was used for the block copolymer directed filler synthesis. Two series of nanocomposites, designated PI-b-PEO-D and PI-b-PEO-E, were studied. Each set contains PEO fractions of 15 and 13 wt%, respectively. The inorganic material consists of a crosslinked sol of 3-glycidoxypropyl trimethoxysilane (CH₃O)₃Si(CH₂)₃OCH₂CHCH₂-O (GLYMO) and aluminum-tri-sec-butoxide Al(OBu^s)₃ in a mol ratio of 4:1 to generate an aluminosilicate ceramic. The synthesis was performed by a PI-b-PEO directed sol-gel synthesis. The PEO block is swollen by the ceramic precursors and acts as a nanoreactor for their sol-gel synthesis. The resulting nanostructured hybrids with PI as the majority phase can be dispersed in an organic solvent to generate objects of spherical, rod-like, or plate-like geometry. PEO acts as an anchor block inside the ceramic phase, and a thin layer of PI 'hairs' covers the resulting nanostructures. The PI-covered nanostructures will then be easily dispersed in a polymeric matrix containing PI due to their compatibility. Figure 2 shows a schematic diagram of the organic-inorganic synthesis. For each series of nanocomposites, the concentration of inorganic component was varied. The synthesis of these nano-materials has been described in detail elsewhere [3,11,12]. The preparation consisted of dissolving 0.5 g of PI-b-PEO copolymer in a 1:1 mixture of chloroform and tetrahydrofuran. Under moderate stirring a prehydrolyzed solution of 4:1 GLYMO:Al(OBu^s)₃ was added, and after 2 hrs the mixture was transferred to a petri dish at 60 to 70°C. The temperature was held for 1 hr for further solvent evaporation. Finally, the formation of the nanocomposite was achieved by applying a heat treatment at ~ 130°C under vacuum for 45 minutes. The procedure was repeated for different concentrations of the metal alkoxide solution in the block copolymer, and thin films of about 0.5 to 1 mm thick were thus obtained; these are listed in Table I.

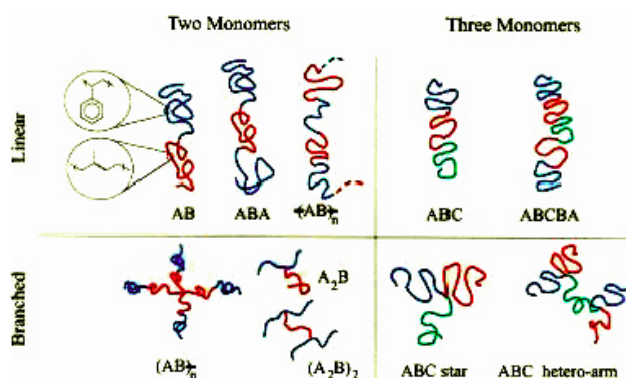


FIGURE 1. Schematic diagram illustrating the classification of block copolymers based on the number of monomer types and topology (linear versus branched sequencing). Each color represents a polymer block composed of a linear sequence of same-type monomers, with monomers types A, B and C shown as blue, red and green, respectively. The insets on the upper-left side show two representative monomer chemical structures.

TABLE I. Block copolymer and hybrid nanocomposites studied in this research. The number average molecular weight was determined by Cornell University.

Sample	Polymer	% PEO	Mass Ratio (inorg/polym)	\bar{M}_n^* (g/mol)
PI-b-PEO	PI-b-PEO-D	15	0	14,200
PD-2	PI-b-PEO-D	15	0.984	14,200
PD-5	PI-b-PEO-D	15	1.21	14,200
PD-10	PI-b-PEO-D	15	1.06	14,200
PE-1	PI-b-PEO-E	13	0.54	29,200
PE-2	PI-b-PEO-E	13	0.51	29,200

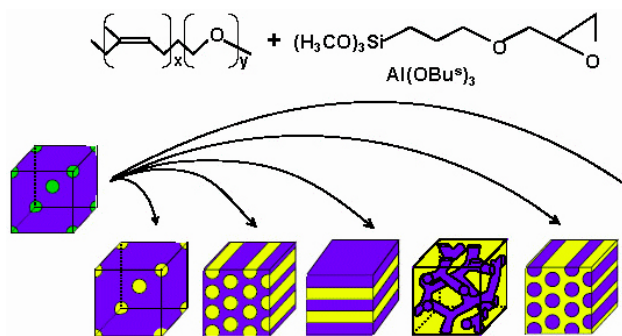


FIGURE 2. Schematic diagram illustrating the synthesis of the inorganic-organic nanocomposites and the possible microphases accessible to these hybrid materials.

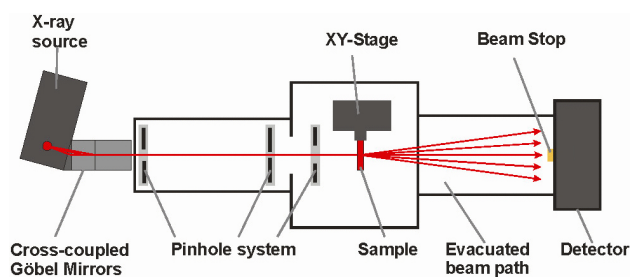


FIGURE 3. Experimental set-up for NanoSTAR U[®] small-angle X-ray scattering system (Bruker-AXS).

2.2. Small-angle X-ray scattering

The morphology of the block copolymer-inorganic nanocomposites was studied using small-angle X-ray scattering (SAXS). Two instruments were utilized:

- (1) 2D SAXS patterns were obtained using the Nanostar U[®] system manufactured by Bruker-AXS. A sealed tube X-ray generator with Cu target (wavelength $\lambda=1.54 \text{ \AA}$) and focal point of $0.4 \times 8 \text{ mm}$ was utilized. The generator was equipped with cross-coupled Göbel mirrors, and it was operated at 40 KV and 35 mA. The SAXS camera works in symmetrical transmission mode using a 3-pinhole collimation system. A sample-to-detector distance of 105 cm was used. The SAXS patterns were recorded using the HiSTAR[®] position sensitive area detector also manufactured by Bruker-AXS. The scattering vector q range attained by this

configuration is $0.01 \rightarrow 0.225 \text{ \AA}^{-1}$. The magnitude of the scattering vector q is defined as

$$q = \frac{4\pi \cdot \sin \theta}{\lambda}, \quad (1)$$

where λ is the radiation wavelength, and θ is Bragg's scattering angle. The experimental setup is shown in Fig. 3.

- (2) 1D SAXS traces were obtained using the 18 KW rotating anode DMAX 2500 X-ray generator (Rigaku Inc). The instrument is equipped with a copper anode (wavelength $\lambda=1.54 \text{ \AA}$). The generator was operated at 50 KV and 200 mA. The SAXS camera works in the symmetrical transmission mode using a 3-slit collimation system and vacuum chamber. The scattered radiation was recorded using a scintillation counter. A Ni-filter is used to filter the 'white radiation' generated by the Cu anode. The sample-to-detector distance is 28.5 cm. The diffraction angle range attained by this configuration is $0.08^\circ 2\theta$ to $2.0^\circ 2\theta$, which translates into a scattering vector q range of $0.0056 \rightarrow 0.143 \text{ \AA}^{-1}$.

2.3. Sample-to-detector distance calibration and background correction

The calibration of the sample-to-detector distance and d -spacing were carried out using silver behenate [13]. Figure 4 shows the SAXS pattern and corresponding azimuthally averaged intensity as a function of the scattering vector. This is a typical Debye-Scherrer pattern and it shows two reflections corresponding to the 001 and 002 peaks. The Debye-Scherrer rings are used to center the position of the incident X-ray beam. On the other hand, the reflection maxima are used to determine the sample-to-detector distance D . Silver behenate shows intensity maxima at $q_{001}=0.1074 \text{ \AA}^{-1}$ and $q_{002}=0.2152 \text{ \AA}^{-1}$, which correspond to a Bragg's d -spacing $d_{001}=58.53 \text{ \AA}$ and $d_{002}=29.19 \text{ \AA}$ [13]. The sample to detector distance D is thus obtained using the relation $\tan 2\theta = r/D$, where r is the distance from the pattern's center to a given reflection, say 001. Based on the first and second order reflections shown in Fig. 4, and carrying out the calibration at least three times, D was determined to be $105 \text{ cm} \pm 0.5\%$. The

contribution of background incoherent scattering due mainly to air scattering was determined by removing a sample from the SAXS camera. The SAXS pattern and corresponding intensity trace thus obtained are shown in Fig. 5. The azimuthally averaged intensity trace shows that parasitic scattering due to the main beam is efficiently eliminated as the background scattering is mostly constant over the entire scattering range, and there is only a slight increase in background contribution in the lower limit 0.01 to 0.03 \AA^{-1} .

2.4. Transmission Electron Microscopy (TEM)

For TEM, the films were stained using osmium tetroxide (OsO_4). The stained samples were embedded in Technovit glue and sectioned at $\sim -50^\circ\text{C}$ using a Reichert cryomicrotome. Ultra-thin sections of about 50 nm were thus obtained. TEM was performed on a LEO 912 Ω (tungsten filament) microscope operated at 120 KV, using an objective

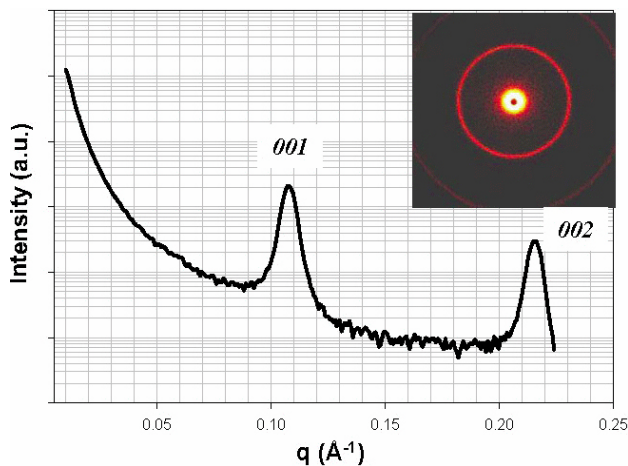


FIGURE 4. SAXS pattern of silver behenate standard and semilogarithmic plot of azimuthally averaged intensity trace as a function of scattering vector q . $\text{CuK}\alpha$ radiation was used.

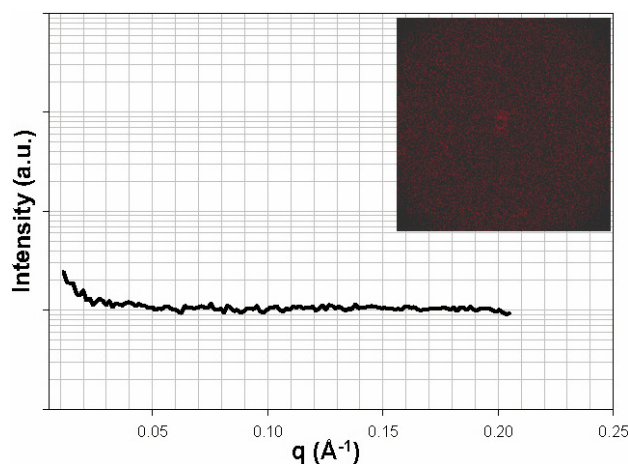


FIGURE 5. Background contribution to SAXS intensity. 2D pattern and azimuthally averaged intensity trace as a function of scattering vector q .

aperture of 120 mrad. Images were recorded using a slow scan CCD camera (lateral resolution $1\text{ K} \times 1\text{ K}$ pixels, 14-bit gray values).

3. Results and discussion

3.1. Microphase separation

Microphase separation is driven by chemical incompatibilities between the different blocks that make up block copolymer molecules. In the simplest case of a diblock copolymer such as PI-b-PEO, there is only the issue of compatibility between the dissimilar isoprene and ethylene oxide blocks. However, note that, unlike binary mixtures of low molecular weight fluids, the entropy of mixing per unit volume of dissimilar polymers is small (varying inversely with molecular weight) [9,10]. Therefore, even minor chemical or structural differences between PI and PEO blocks are sufficient to produce excess free-energy contributions that are usually unfavorable to mixing.

If the blocks of a copolymer melt were not connected by covalent bonds to each other, the thermodynamic forces would lead to a *macrophase* separation. Macrophase separation is a state of coexistence of bulk phases, *e.g.*, oil and vinegar separate into macroscopically-sized droplets in a salad dressing. In a block copolymer, however, entropic forces from the covalent linkages counterbalance the thermodynamic forces driving phase separation. These forces (also called chain elasticity) reflect the requirement that, to keep the dissimilar PI and PEO portions of each molecule apart, copolymers must adopt extended configurations. As there are fewer configurations available to extended polymer chains than those in their native randomly coiled state, an entropy-restoring force is generated that serves to limit the phase separation between PI and PEO blocks to mesoscopic dimensions. The entropic force law is approximately Hookean, and provides the basis for understanding the elasticity of rubber-like materials [10].

3.2. Diblock copolymer microphases

The parameters that characterize the block molecular structure are:

- (1) the overall degree of polymerization N , which is the total number of monomers per macromolecule, and
- (2) the composition $f_A = N_A/N$, where N_A is the number of A monomers per macromolecule [10].

For a symmetric diblock, $f_A = f_B = 1/2$. At low temperatures (large χ_{AB}), the segregation is strong, leading to microdomains that are nearly pure in A and B, separated by interfaces that are much narrower than the *lamellar* domain period λ . This microphase separation is achieved provided that the symmetric diblock copolymers have high enough molecular weight or that these are strongly incompatible blocks. Let

us point out that mean-field theories have been used to predict the phase diagram of diblock copolymers, including the order-disorder transition (ODT), and the results compare well with experimental phase diagrams [9]. However, this topic is beyond the scope of this work and will not be discussed any further.

As stated above, the *lamellar* (L) microphase is stable for nearly symmetrical diblocks, while a *hexagonally packed cylinder* (C) phase is stable for diblocks with intermediate levels of compositional asymmetry. When $f_A < 1/2$, the smaller A blocks pack into the interiors of cylinders. This energetically preferable configuration allows the longer B blocks to reside on the convex side of the A-B interface, which affords them more configurational entropy (or reduction of the elastic energy). With still more compositional asymmetry, the hexagonal phase gives way to a *body-centered cubic spherical* (S) microphase. There are two more microphases in diblock copolymers that have been predicted, and observed, namely the perforated layers (PL) and the gyroid (G) microphases [9,10].

The SAXS trace of the neat copolymer PI-b-PEO with 15 wt% PEO ($f_{PEO}=0.15$) is shown in Fig. 6a. The characteristic morphology of the discontinuous domains in the neat copolymer and in their nanocomposites was determined from the scattering vector q values of higher order reflections relative to the first-order reflection. Note that, due to the composition of the block copolymer, a body-centered cubic spherical microphase would be favored. This is indeed the case; the intensity trace in Fig. 6a shows a first-order reflection at $q \approx 0.0406 \text{ \AA}^{-1}$, which corresponds to a spacing of $d = 154.6 \text{ \AA}$ ($d = 2 \cdot \pi / q$). There are also higher order reflections which are positioned at 0.0578, 0.07031 and 0.1078 \AA^{-1} . These correspond to spacings of 108.7, 89.4 and 58.3 \AA . The positions of the secondary maxima relative to the first-order reflection follow the scaling: $2^{1/2}$, $3^{1/3}$ and $7^{1/2}$. The scaling corresponds to a cubic spherical nanophase [9] in the neat PI-b-PEO $f_{PEO}=0.15$ copolymer. The correct assignment of morphology was corroborated by TEM, Fig. 6b. The contrast in the micrograph arises from the stained poly-isoprene domains by OsO_4 and these appear black. TEM indeed confirms the spherical nanophase separation in the neat block copolymer PI-b-PEO $f_{PEO}=0.15$.

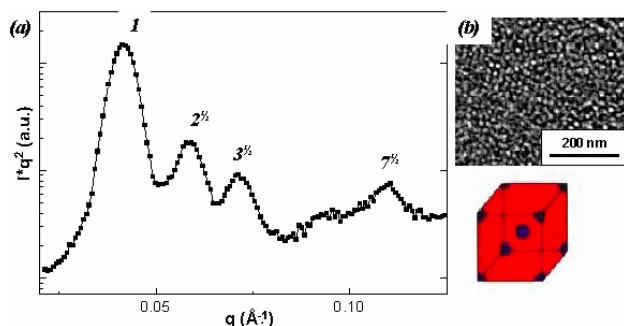


FIGURE 6. SAXS intensity trace of parent PI-b-PEO block copolymer with $f_{PEO}=0.15$. The positions of the intensity maxima correspond to a cubic spherical symmetry.

TABLE II Intensity maximum position (in nanometers) obtained from SAXS patterns. Scaling corresponds to lamellar nanophase.

Sample	Lamellar	1	2	3	4	5
PD-2	Observed	33.9	16.8	11.3	8.1	6.2
	Theoretical	33.9	16.9	11.3	8.5	6.7
PD-5	Observed	22.5	10.9	7.6	-	-
	Theoretical	22.5	11.2	7.5	-	-
PD-10	Observed 1	21.2	11.2	7.1	5.9	-
	Theoretical	21.2	10.6	7.1	5.3	-

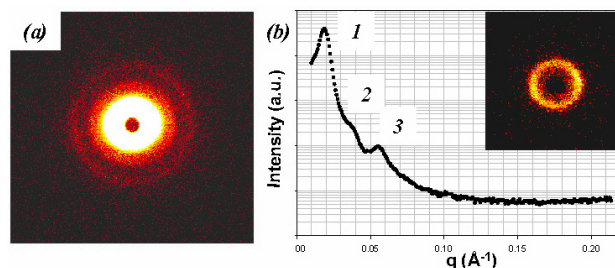


FIGURE 7. (a) SAXS pattern of nanocomposite PD-2. The second- and third-order reflections can be easily appreciated. Pattern obtained after 1000 s exposure (b) Azimuthally averaged intensity trace as a function of scattering vector q . The inset shows the SAXS pattern obtained after 10 s exposure.

3.3. Nanophase in hybrid nanocomposites

The microstructural analysis carried out shows that, despite the cubic microphase being favored by the pure block copolymer with $f_{PEO}=0.15$, the inclusion of the inorganic material greatly influences the morphology of the nanocomposite. Figure 7a shows the 2D SAXS diffraction pattern for the PD-2 nanocomposite containing $f_{PEO}=0.15$ and an inorganic-organic mass ratio of 0.98. The pattern, obtained after 1000 s exposure, shows a series of Debye-Scherrer rings, confirming the existence of *microphase separation* in the hybrid nanocomposite. The intensity around the azimuth is mostly uniform, and indicates that there is no preferred orientation in the plane of the film. Figure 7b shows the azimuthally averaged intensity trace of the pattern. The 2D SAXS pattern shown as an inset in Fig. 7b was obtained after a 10 s exposure; note that the inner first-order reflection that is overexposed in Fig. 7a is now clearly resolved. The intensity trace shown in Fig. 7b shows higher-order maxima, indicating that there is long-range order in the hybrid material. Strikingly, the positions of the secondary maxima are integer multiples of the first-order reflection (labeled as *I*), indicating the existence of alternating *lamellar* microdomains with a long-range spatial order. A lamellar morphology results in relative q values of $q_i = 1, 2, 3, 4, \dots$ [9]. The observed positions of each reflection for PD-2 (in units of nm) followed by theoretical maxima positions, are listed in Table II. The theoretical positions are obtained by dividing the scattering vector of the

TABLE III. Intensity maximum position (in nanometers) obtained from SAXS patterns. Scaling corresponds to hexagonal cylindrical nanophase.

Sample	Hexagonal cylindrical	1	$5^{1/2}$	$7^{1/2}$	$13^{1/2}$	$15^{1/2}$
PE-1	Observed	48.5	-	18.1	-	12.3
	Theoretical	48.5	18.3	12.5		
PE-2	Observed	33.9	16.6	12.9	9.2	-
	Theoretical	33.9	15.1	12.8	9.4	

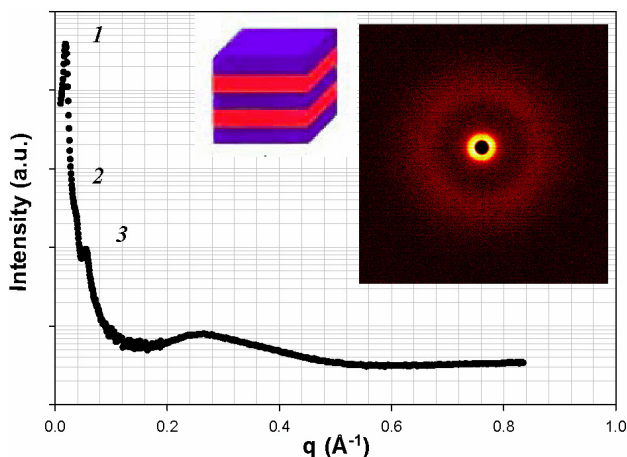


FIGURE 8. Wide-angle X-ray scattering pattern of nanocomposite PD-2 and merged azimuthally averaged intensity traces obtained in the SAXS and WAXS configurations. The wide-angle amorphous halo demonstrates that there is no crystalline order in the material.

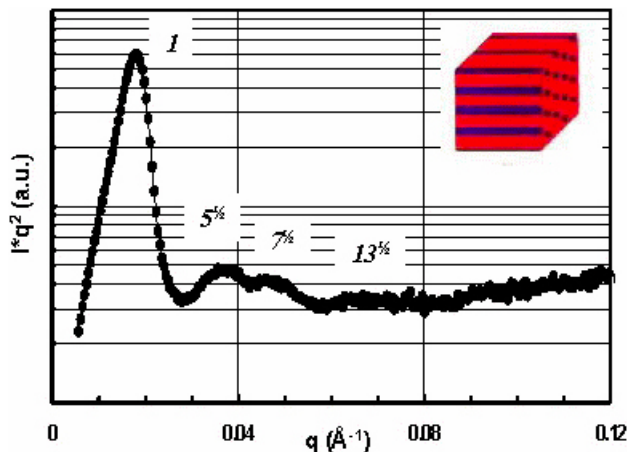


FIGURE 9. SAXS intensity trace of hybrid nanocomposite PE-2 (PI-b-PEO-E). Fraction of PEO is 0.13 and inorganic-to-organic mass ratio is 0.51. The periodic nanostructure describes a cylindrical morphology.

first order maximum by the factor shown at the top of each column.

Thus, these results have shown that the inorganic nanofiller not only preserves the long-range spatial order characteristic of monodisperse block copolymers, but the nanophase in the hybrid nanocomposite is now driven by the

amount of nanofiller, not by the composition of the parent block copolymer.

The short range order was investigated by using wide-angle X-ray scattering (WAXS). The WAXS pattern of PD-2 is shown in Fig. 8. This pattern shows only an amorphous halo with maximum intensity at $q \approx 0.26 \text{ \AA}^{-1}$ that corresponds to an average intermolecular correlation of 24.2 \AA . The merged azimuthally-averaged intensity trace obtained from the SAXS and WAXS techniques is also shown in Fig. 8. The intensity trace shows clearly the existence of a long-range nanoscopic order, and this does not imply spatial order at the intermolecular scale.

The SAXS results from the PD-5 and PD-10 nanocomposites also showed an integer scaling in the position of the diffraction maxima. Therefore, one concludes that these nanocomposites also exhibit lamellar morphology. The observed position of each reflection for these samples, followed by the respective theoretical maximum positions, is listed in Table II.

Figure 9 show the SAXS diffraction pattern for the nanocomposite PE-2, which corresponds to the block copolymer PI-b-PEO with $f_{PEO}=0.13$ and an inorganic-to-organic mass ratio of only 0.51. The pattern exhibits multiple scattering maxima that follow to the scaling $q_i=1, 3^{1/2}, 4^{1/2}, 7^{1/2}, 9^{1/2}, 12^{1/2} \dots$ relative to that of the first-order reflection. The maximum positions imply the existence of hexagonally-packed cylindrical microdomains, with long-range spatial order [9]. Due to composition considerations, it is suggested that the PEO-inorganic material forms the cylindrical microdomains. The SAXS pattern of the hybrid PE-1 also describes to a cylindrical microdomain. The observed position of each reflection for PE-1 and PE-2, followed by theoretical maximum positions, are listed in Table III.

3.4. Interdomain spacing

From the SAXS analyses, one can determine the *average interdomain distance* D , *i.e.* the domain identity period for the lamellae, the nearest-neighbor distance between the microdomains for the cylinders and the spheres, and the *average radius* R of cylinders or spheres. The interdomain distance D can be determined from the corresponding Bragg spacings [9], for instance, for lamellar microdomains $D = d_{001}$; for hexagonally-packed cylindrical microdomains $D = \sqrt{4/3} \cdot d_{100}$; and for the spherical microdomains, with simple cubic (sc) symmetry $D = d_{100}$ and for body-centered cubic (bcc) symmetry $D = \sqrt{3/2} \cdot d_{110}$. The Bragg spacing is determined from the multiple-order diffraction maxima (for instance, for lamellar microdomains $2d_{00l} \cdot \sin \theta_{00l} = \lambda$, where $l = \text{integers}$ and $d_{00l} = D/l$).

Diffraction maxima associated with isolated particle scattering were not observed in the SAXS traces. However, it is noted that the radius of the cylinders (spheres) in the nanodomains can still be determined from space filling considerations, based on the geometry of the microphase (*i.e.* hexagonal cylindrical or cubic), and the volume fraction of the minor

phase, $\phi_{PEO-ceramic}$ [14]. The relations between volume fraction, ϕ , and the radius, R , of the microdomains for each given morphology are reported elsewhere [15]. The characteristic morphology, the values of the spacing d , and the interdomain spacing D estimated directly from the diffraction patterns are summarized in Table IV.

3.5. Nanophase morphology by TEM

To corroborate the correct assignment of the SAXS patterns to a lamellar and a cylindrical morphology, the hybrid nanocomposites were also examined by transmission electron microscopy (TEM). Figure 10 shows the TEM micrographs corresponding to samples PD10 and PE2. The contrast in these micrographs arises from the poly-isoprene, stained with osmium tetroxide (OsO_4) and appearing black. The micrograph of PD10 (Fig. 10a) clearly shows lamellae. On the other hand, the micrograph of PE2 (Fig. 10b) shows hexagonally packed cylinders in the two most typical projections. Note the smaller distance in the lamellar and hexagonal spacing in the TEM micrographs (12 and 28 nm, respectively) relative to that indicated by the SAXS results (see Tables II and III). This is a result of the contraction of the ultrathin sections normal to the plane of the nanophases which is driven by free energy minimization [16].

TABLE IV. The characteristic nanophase, the values of the spacing d , and the interdomain spacing D of hybrid nanocomposites calculated directly from SAXS data.

Sample	First order q (nm^{-1})	d (nm)	D (nm)	Morphology
PI-b-PEO	0.406	d_{100} or	15.46	Cubic, sc
		$d_{110}=15.46$	18.9	Cubic, bcc
PD-2	0.181	$d_{001}=33.9$	33.9	Lamellar
PD-5	0.279	$d_{001}=22.5$	22.5	Lamellar
PD-10	0.296	$d_{001}=21.2$	21.2	Lamellar
PE-1	0.129	$d_{100}=48.5$	56.0	Cylindrical
PE-2	0.185	$d_{100}=33.9$	39.2	Cylindrical

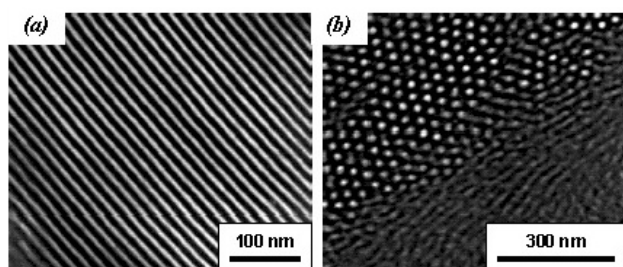


FIGURE 10. Transmission electron microscopy images of (a) PD10 and (b) PE2 hybrid nanocomposites.

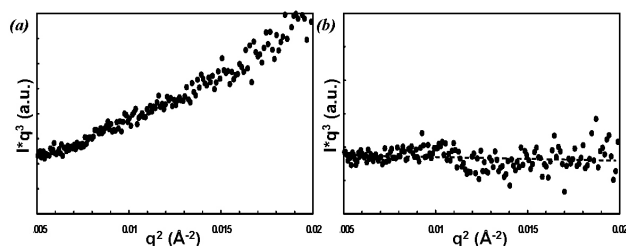


FIGURE 11. Plot of $I \bullet q^3$ as a function of q^2 for (a) PE-2 and (b) PD-2. These are typical positive and negative deviations from Porod's law.

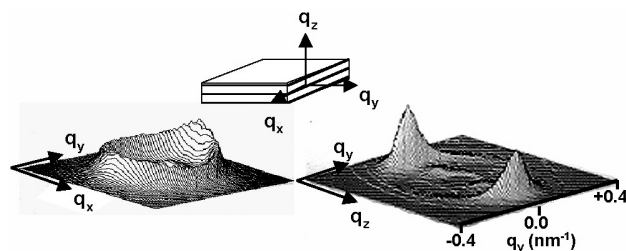


FIGURE 12. Three-dimensional SAXS patterns of PD10 hybrid nanocomposite for two different directions of the X-ray beam with respect to the sample coordinate frame, as schematically depicted in the inset. Intensities are not normalized.

3.6. Nanophase boundaries

Porod analysis was carried out on the SAXS data using a protocol derived by Koberstein *et al.* [17]. Positive deviations from Porod's law were observed in plots of $q^3 \bullet I$ as a function of q^2 for samples PD-10, PE-1 and PE-2; Fig. 11a shows typical results. The positive slope in the high angle range suggests the presence of sharp boundaries among the nanophases, and the possible presence of isolated phase mixing. This is correlated with the TEM results. On the other hand, negative deviations from Porod's law were observed for samples PD-2 and PD-5, Fig. 11b. These results suggest that the boundaries among the nanophases for these samples are diffuse.

3.7. Orientational effects

Finally, we discuss the orientational effect induced by the solvent-cast method, which is part of the preparation procedure of these materials. Three-dimensional (3D) SAXS patterns for two different orientations of a film of PD2 sample (which exhibits a lamellar nanophase) with respect to the X-ray beam are shown in Fig. 12. The patterns are not normalized in order to enhance their features. When the X-ray beam is directed along the q_z axis, the results show that, in the q_x - q_y plane (the film plane), only a ring of continuous intensity is observed. However, when the X-ray beam is directed along the q_x (or q_y) axis, the results show that in the q_y - q_z plane there are two strong, narrow peaks. These peaks are positioned on the q_z axis, and this result indicates that the lamellae are oriented parallel to the surface of the film. The results demonstrate that the solvent-cast technique is able

to induce macroscopically aligned samples for the lamellar hybrid nanostructure. We note that the film thicknesses of these samples is significant (~ 1 mm), and therefore surface-induced morphological transitions and related effects for very thin films can be neglected [18].

4. Conclusions

The results of this investigation have demonstrated that the use of a block copolymer as a nanostructure directing agent permits the synthesis of hybrid (organic-inorganic) nanocomposites with well-defined, reproducible and highly ordered nanostructures. The type of nanoscopic symmetry achieved mimics the behavior of neat block copolymers and is a function of the concentration of inorganic nanofiller. Small-angle X-ray scattering (SAXS) is an adequate technique for characterizing the morphology and microdomain size in these block copolymer-inorganic nanostructures. Moreover, SAXS can

give more accurate values for the nanostructural distances than, say, TEM –transmission electron microscopy– due to the radiation damaged caused by TEM, which leads to the shrinkage of the samples and their inner distances. Finally, understanding block copolymer directed nanoassembly at a fundamental level may also be of key importance for developing specific architectures over extended length scales for a wide range of inorganic materials.

Acknowledgements

The author would like to thank Brüker-AXS for making available the NanoSTAR U[®] system, and Prof. U. Wiesner (Max-Planck-Institut für Polymerforschung) for TEM micrographs and enlightening discussions. The author gratefully acknowledges the financial support of the Mexican Council for Science and Technology (CONACyT) and the Coordinación de la Investigación Científica-UNAM.

*. Presented at the “Mexican Workshop on Nanostructured Materials”, Puebla Pue., México, 2-4 May, 2006.

1. B. Chen, *British Ceramic Trans.* **103** (2004) 241.
2. G. Decher, *Science* **277** (1997) 1232.
3. M. Templin *et al.*, *Science* **278** (1997) 1795.
4. B.R. Haywood and S. Mann, *Adv. Materials* **6** (1994) 9.
5. C.T. Kreage, M.E. Leonowicz, W.J. Roth, J.C. Vartuli, and J.S. Beck, *Nature* **359** (1992) 710.
6. S. Mann and G. Ozin, *Nature* **382** (1996) 313.
7. L. Mercier and T.J. Pinnavaia, *Adv. Materials* **9** (1997) 500.
8. Z-R. Chen, J.A. Kornfield, S.D. Smith, J.T. Grothaus, and M.M. Sattkowski, *Science* **278** (1997) 1248.
9. I.W. Hamley, *Block Copolymers* (Oxford University Press, England, 1998).
10. R.G. Larson, *The Structure and Rheology of Complex Fluids* (Oxford University Press, Oxford, 1999).
11. A. Jain *et al.*, *Macromolecules* **35** (2002) 4862.
12. R. Ulrich, A. Du Chesne, M. Templin, and U. Wiesner, *Adv. Mater.* **11** (1999) 141.
13. T. C. Huang, H. Toraya, T.N. Blanton, and Y. Wu, *J. Appl. Cryst.*, **26** (1993) 180.
14. R.F. Storey and D.W. Baugh III, *Polymer* **41** (2000) 3205.
15. S. Sakurai, H. Kawada, T. Hashimoto, and L.J. Fetters, *Macromolecules* **26** (1993) 5796.
16. A. DuChesne, PhD Thesis, University of Mainz (1993).
17. J.T. Koberstein, B. Morra, and R.S. Stein, *J. Appl. Cryst.* **13** (1980) 34.
18. Y. Liu, M.H. Rafailovich, J. Sokolov, S.A. Schwarz, and S. Bahal, *Macromolecules* **29** (1996) 899.